The North Galactic Pole Rift and the Local Hot Bubble

S. L. Snowden, Dimitra Koutroumpa, K. D. Kuntz, Rosine Lallement, L. Puspitarini

The Astrophysical Journal, 806:120 (8pp), 2015 June 10 doi:10.1088/0004-637X/806/1/120

THE NORTH GALACTIC POLE RIFT AND THE LOCAL HOT BUBBLE

S. L. Snowden[1], D. Koutroumpa[2], K. D. Kuntz[3], R. Lallement[4], and L. Puspitarini[5]
[1] NASA/Goddard Space Flight Center, Greenbelt, MD 20771, USA
[2] Université Versailles St-Quentin; Sorbonne Universités, UPMC Univ. Paris 06; CNRS/INSU, LATMOS-IPSL, 11 Boulevard d'Alembert, F-78280, Guyancourt, France
[3] The Johns Hopkins University, The Henry A. Rowland Department of Physics and Astronomy, Baltimore, MD 21218, USA
[4] GEPI, Observatoire de Paris, CNRS UMR8111, Université Paris Diderot, 5 Place Jules Janssen, F-92190 Meudon, France
[5] Bosscha Observatory and Department of Astronomy, FMIPA, Institut Teknologi Bandung, Jl. Ganesha 10, Bandung 40132, Indonesia
Received 2015 March 23; accepted 2015 April 20; published 2015 June 12

ABSTRACT

The North Galactic Pole Rift (NGPR) is one of the few distinct neutral hydrogen clouds at high Galactic latitudes that have well-defined distances. It is located at the edge of the Local Cavity (LC) and provides an important test case for understanding the Local Hot Bubble (LHB), the presumed location for the hot diffuse plasma responsible for much of the observed 1/4 keV emission originating in the solar neighborhood. Using data from the *ROSAT* All-Sky Survey and the Planck reddening map, we find the path length within the LC (LHB plus Complex of Local Interstellar Clouds) to be 98 ± 27 pc, in excellent agreement with the distance to the NGPR of 98 ± 6 pc. In addition, we examine another 14 directions that are distributed over the sky where the LC wall is apparently optically thick at 1/4 keV. We find that the data in these directions are also consistent with the LHB model and a uniform emissivity plasma filling most of the LC.

Key words: ISM: bubbles – ISM: clouds – ISM: magnetic fields – solar neighborhood – X-rays: diffuse background

1. INTRODUCTION

The bulk of the cosmic soft-X-ray background (SXRB) observed at 1/4 keV likely originates as thermal emission from a diffuse $\sim 10^6$ K plasma contained within the Local Cavity (LC, Knapp 1975) in the H I of the Galactic disk surrounding the Sun. This region is called the Local Hot Bubble (LHB, e.g., Sanders et al. 1977; Tanaka & Bleeker 1977; Cox & Snowden 1986; Snowden et al. 1990) and extends from a few tens of parsecs in the Galactic plane to 100–200 pc (or more) at high Galactic latitudes. The acceptance of the LHB model over the years has not been without debate (e.g., Welsh & Shelton 2009), however, recent results have provided strong support for its existence (Galeazzi et al. 2014; Snowden et al. 2014; Snowden et al. 2015b, hereafter Paper I).

The basic premise for the LHB model is that the local 1/4 keV background arises from a uniformly distributed hot plasma within the LC implying that the observed intensity should be proportional to the plasma path length. In practice, any analysis is complicated by heliospheric X-ray emission from solar wind charge exchange (SWCX, see Cravens et al. 2001; Robertson & Cravens 2003; Lallement 2004; Snowden et al. 2004; Wargelin et al. 2004) and background X-ray emission from other regions in the Galactic disk, the Galactic halo, and beyond. These two sources of "contamination" are of interest in their own right, and are also tractable as it is possible to model the SWCX contribution (see Kuntz et al. 2015, for an extensive discussion on this subject) and to use shadowing by distinct clouds in the interstellar medium to separate the observed intensity into foreground and background components, relative to the cloud.

Two recent papers have derived consistent average plasma pressures for the LHB. Puspitarini et al. (2014) used the local 1/4 keV component map of Snowden et al. (1998), the three-dimensional local interstellar medium dust maps of Lallement et al. (2014), and simple assumptions about the homogeneous filling of dust-free regions by 10^6 K gas. Snowden et al. (2014) used the 1/4 keV *ROSAT* All-Sky Survey (RASS) map of Snowden et al. (1997), the same dust maps, and the results of Galeazzi et al. (2014, hereafter GEA14) that derived an estimate for the residual SWCX contribution to the RASS. The results were in good agreement with plasma pressures of 10,200 cm^{-3} K and 10,600 ± 1070 cm^{-3} K, respectively. Paper I used these results to study the line of sight (LOS) toward the Local Leo Cold Cloud (LLCC; a nearby interstellar cloud embedded in the LHB) that was thought to cast doubt on the existence of the LHB (Peek et al. 2011). Paper I found that with our current understanding of heliospheric SWCX, the emission originating foreground and background to the cloud was indeed consistent with the uniform plasma of Puspitarini et al. (2014) and Snowden et al. (2014).

In this paper we extend the analysis to 15 new directions using the methods of Paper I, and rely on Paper I (and references therein) for detailed descriptions of the issues involved (SWCX emission, shadowing, and the dependency of band-averaged absorption cross sections on column density). We consider only the 1/4 keV band because the LHB emits primarily, if not exclusively at those energies, the statistics of the RASS 1/4 keV maps far exceed those of the higher energy bands, and the SWCX background can be more accurately modeled at 1/4 keV (Kuntz et al. 2015). In Section 2 we analyze in detail the North Galactic Pole Rift (NGPR), in Section 3 we consider additional directions where the LC wall is optically thick or the shadowing analysis has already been published. In Section 4 we present our conclusions.

2. NORTH GALACTIC POLE RIFT

The NGPR is a well-defined H I feature at $l, b \sim 315°, 84°$ (Figure 1, upper panels), which lies between the Coma and Virgo clusters of galaxies and just outside of the North Polar Spur (NPS) X-ray enhancement. It is also known as

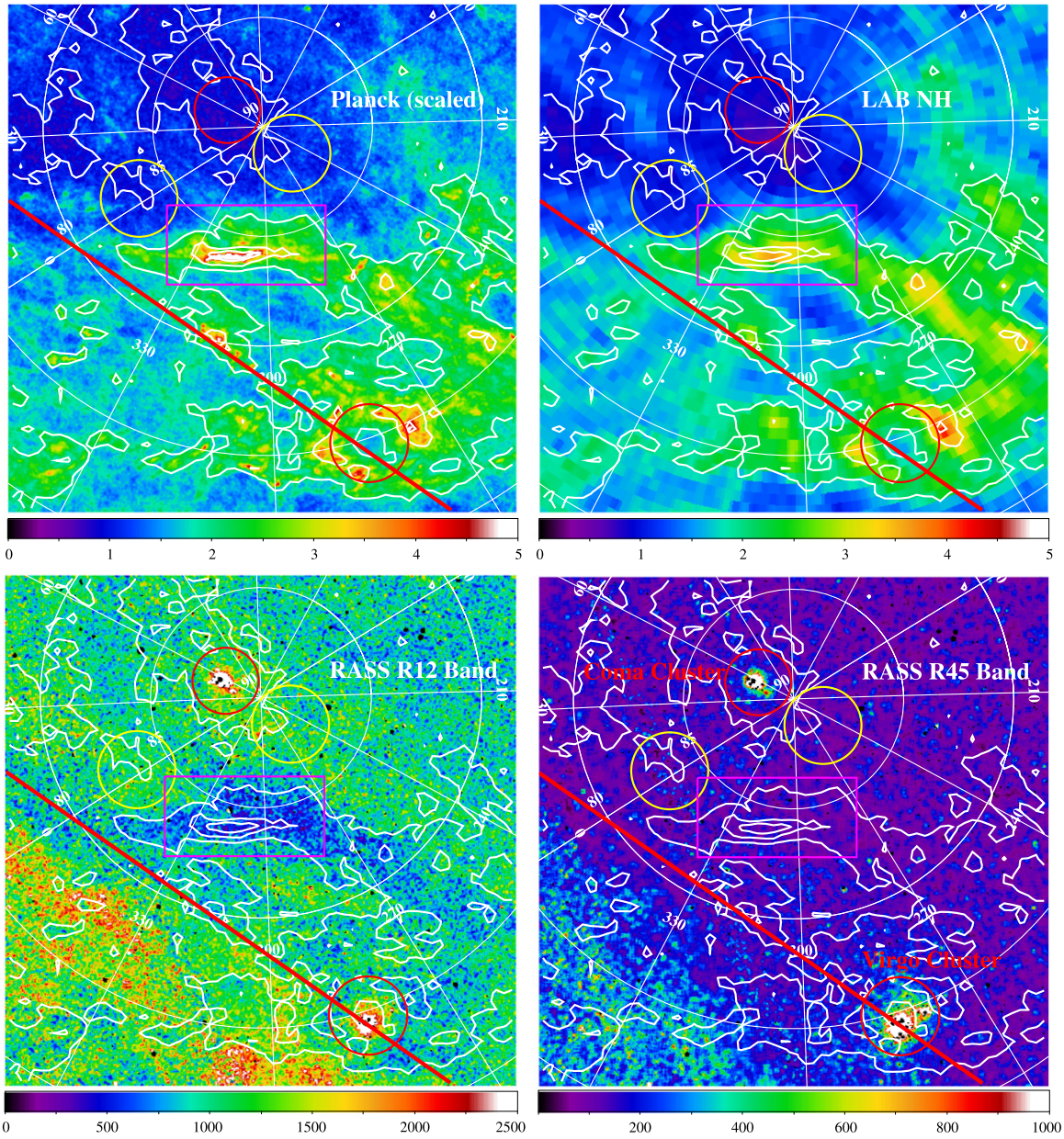

Figure 1. (Upper left) scaled Planck reddening $E(B-V)$ image of the region with the color bar in units of 10^{20} cm^{-2}. The upper red circle encloses the Coma cluster, the lower right circle encloses the Virgo cluster, the two yellow circles show the extraction regions for the spectral analysis, and the magenta box shows the region used for the shadowing analysis. The red line roughly indicates the extent of the NPS emission. (Upper right) H I column density of the region from the LAB survey ($v < |250|$ km s^{-1} with the color bar in units of 10^{20} cm^{-2}). (Lower left) Smoothed RASS R12 (1/4 keV) band data of the region with the color bar in RU (*ROSAT* units, 10^{-6} counts s^{-1} arcmin^{-2}). (Lower right) smoothed RASS R45 (3/4 keV) band data of the region with the color bar in RU. All fields cover the same region and the contours are from the scaled Planck data with levels at 1, 2, 3, and 4×10^{20} cm^{-2}. The coordinate grid is in galactic coordinates.

Markkanen's cloud (Markkanen 1979), and has been studied in the interstellar polarization of optical light (e.g., Berdyugin & Teerikorpi 2002). The distance to the NGPR was determined by Puspitarini & Lallement (2012) to be 98 ± 6 pc using the presence or absence of interstellar absorption lines in the spectra of stars distributed along the NGPR LOS. Because it lies at such a high Galactic latitude it provides an interesting test for the LHB model as the distance to the boundary of the LC is in general ill-defined toward the poles, possibly resembling more of a chimney than an enclosed cavity (Welsh et al. 1999). The NGPR is clearly seen as a shadow in the RASS 1/4 keV image of the region (Freyberg & Breitschwerdt 2001) but is not sufficiently thick or extensive to be readily observed at 3/4 keV in the RASS data (Figure 1, lower left and lower right panels, respectively).

2.1. Planck and LAB Data

As in Paper I, we use the Planck reddening map (Planck Collaboration et al. 2014) scaled to a column density of H I using the Leiden/Argentina/Bonn 21 cm survey (LAB, a merging the Leiden/Dwingeloo Survey, Hartmann & Burton 1997, and the Instituto Argentino de Radioastronomía Survey, Arnal et al. 2000; Bajaja et al. 2005) to provide a high angular resolution surrogate for the X-ray absorption column

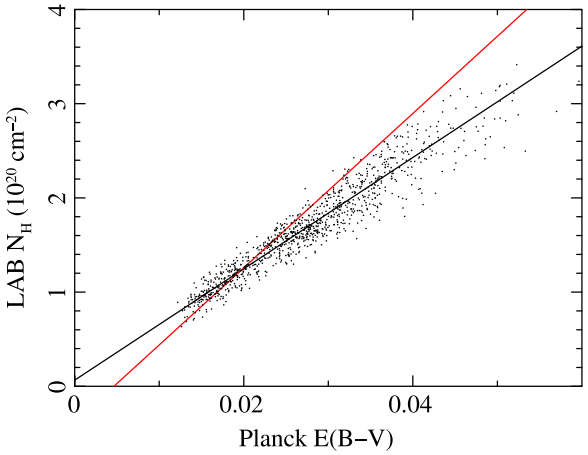

Figure 2. Scatter plot of LAB NH vs. the Planck $E(B-V)$ data. The first order polynomial fit was restricted to reddening values <0.04. The result is the relation $N_H = 0.065 + 59.1 \times E(B-V)$ (where N_H is in units of 10^{20} cm^{-2}). The black line shows the fit for these data while the red line shows the fit for the data from the region analyzed in Paper I.

density. Figure 2 shows a scatter plot of LAB data versus Planck $E(B-V)$ data for the region covered in Figure 1 after binning into $30' \times 30'$ pixels. The data show a tight correlation between the two quantities with much of the scatter likely due to the radical difference between the angular resolution of the two surveys (few arcminutes versus half a degree).

We use the fitted relation (for Planck $E(B-V) < 0.04$ to avoid the effect of any molecular hydrogen) of $N_H = 0.065 + 59.1 \times E(B-V)$ in units of 10^{20} cm^{-2} to scale the Planck data (black line in Figure 2). We note that this relation is significantly different than that found in Paper I (i.e., $N_H = -0.38 + 81.9 \times E(B-V)$ in the same units, shown by the red line in Figure 2). However, while this may suggest a dependence on Galactic latitude and height above the plane (the two directions are at $b = 84°$ and $b = 45°$), we use the locally derived relationship below and leave the interpretation of the variation for other investigations.

2.2. RASS Data

For the NGPR analysis we recast the RASS data (published with $12' \times 12'$ pixels) into images with $2\farcm7 \times 2\farcm7$ pixels to better match their intrinsic angular resolution, as well as the resolution of the Planck data ($\sim 5'$). With this pixel size the data are undersampled so for the maps in Figure 1 the data are adaptively smoothed. For the shadow analysis (the correlation between column density and X-ray intensity) the X-ray data (observed counts, exposure, and model background counts) are combined into 0.1×10^{20} cm^{-2} H I column density bins. Each bin then represents the average X-ray intensity over the field for that column density.

The SXRB in the region surrounding the NGPR has a complex structure with variations due to both changes in the plasma emission measure and absorption by the varying column density of Galactic H I. The NPS (the strong enhancement in the lower left of the X-ray images, e.g., Borken & Iwan 1977) is thought to be the limb-brightened edge of the Loop I superbubble (or, alternatively, a supershell centered on the Galactic center, Sofue 2000). The Virgo and Coma clusters of galaxies contribute enhancements of more limited extent (for amusement, note the relatively well-defined ring of Galactic H I surrounding the Virgo cluster). The effect of shadowing is clearly apparent in a casual comparison of the Figure 1 Planck and RASS 1/4 keV maps (upper left and lower left panels, respectively).

2.3. Shadowing Analysis

For the shadowing analysis of the NGPR we can simplify the method used in Paper I, where the shadowing target was contained within the X-ray emitting plasma of the LHB. Here we assume that the NGPR is embedded within the wall forming the boundary of the LC and that there are only two emission regions, one foreground and one background to the total Galactic column density of H I. The radiative transfer equation simplifies to:

$$I = I_0 + I_1 \times e^{-N_H \times \sigma(N_H)}$$

where I is the observed intensity, I_0 is the foreground LHB plus SWCX intensity, and I_1 is the distant intensity originating beyond the Galactic H I. N_H is the Galactic H I column density as measured by the scaled Planck reddening data. The X-ray band average effective cross section, $\sigma(N_H)$, is dependent on the shape of the incident spectrum as well as the absorption column density (see Paper I). The use of the band-averaged effective cross section rather than a constant cross section in the analysis is crucial as the use of the latter will result in a derived foreground intensity larger than the true value.

Similar to the Paper I analysis, we fit a standard four component model to the RASS spectra from two low N_H regions directly adjacent to the NGPR (the yellow circles in Figure 1). The regions were chosen because of their proximity to the NGPR and their low and relatively constant column densities. The four components are the SWCX plus LHB emission with $kT \sim 0.09$ keV, an absorbed cooler Galactic halo component tied to the same kT, an absorbed hotter Galactic halo component with $kT \sim 0.23$ keV, and an absorbed power law with a fixed index of 1.46 (the extragalactic background comprised primarily of the emission from unresolved active galactic nucleus). The temperatures and normalizations of the fitted absorbed components of the spectrum were then used with the spectral modeling program Xspec (Arnaud 1996) to parametrize the magnitude of the transmitted flux as a function of absorption column density to create a model absorption curve for use in fitting the shadowing relation. This was done iteratively (fitting the spectra, determining the absorption curve, then fitting the shadowing relation) by varying the normalization of the local component in the spectral fit until the intensity of the local component of the spectral fit agreed with the intensity of the local component of the shadowing analysis to better than 1 RU. For reasons discussed below (the likely existence of residual contamination in the RASS data), we used the data from the left half of the NGPR region for this iterative process. However, the choice of region has $<0.5\sigma$ effect on the fitted shadowing intensities.

The data from the entire region indicated by the magenta box in Figure 1 were fit with the absorption curve (see Table 1 and Figure 3) with problematic results. As shown in the residual map of Figure 4 (left panel), there is a distinct left side/right side asymmetry. To investigate this further, we split the region into halves, refit the data, and found a 25% difference in the fitted foreground intensity (again, see Table 1 and Figure 3). There are two issues that lead to the right half/left half

Table 1
Shadow Fit Parameters

Parameter	Full Region (RU)	Left Half (RU)	Right Half
Foreground Intensity (I_0)	346 ± 14	398 ± 18	294 ± 23
Background Intensity (I_1)	2556 ± 86	2407 ± 112	2673 ± 163
χ^2	76.5	89.3	32.4
Degrees of Freedom (ν)	61	61	38
Reduced χ^2 (χ^2_ν)	1.25	1.46	0.8

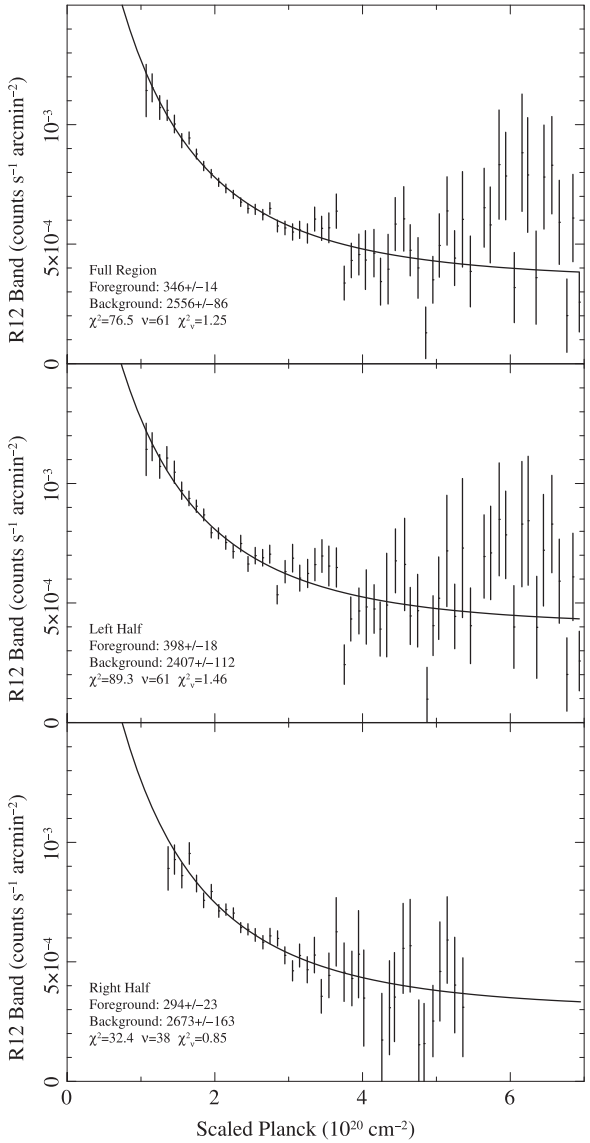

Figure 3. Scatter plot of RASS R12 band surface brightness vs. the Planck reddening data scaled to units of H I column density (see the text for details). The data have been binned in steps of 0.1×10^{20} cm^{-2}. Top panel: the fit includes all data from within the region. Middle panel: the fit includes data from only the left half of the region. Bottom panel: the fit includes data from only the right half of the region.

discrepancies seen in the fitted parameters. First, noticeable in the full region and left-side fits, the intensity at lower column densities ($N_{\rm H} < 5 \times 10^{20}$ cm^{-2}) falls off as expected but at higher columns this does not appear to be the case. However, for the left side fit limiting the fit range to $N_{\rm H} < 5 \times 10^{20}$ cm^{-2} has a negligible effect on the fitted foreground intensity ($<1\sigma$). Second, as noted above, the surface brightness on the right side of the NGPR field is generally lower than on the left side. This is of greater concern, and (again) is obvious in Figure 4 (left panel) which shows the difference between the data and the fitted absorption model. The RASS exposure map (Figure 4, right panel) provides some insight. The diagonal streaking of the exposure indicates the scanning direction of the survey, and shows that the right side of the region was covered in the same scans as the Virgo and Coma clusters. This is unfortunate as the brightness of the clusters may have affected the accuracy of the empirical "long-term enhancement" analysis (Snowden et al. 1995), as magnetospheric SWCX was designated at that time. This likely led to an over-subtraction of the background.

2.4. SWCX Analysis

Following the method detailed in Paper I, we estimate the residual contribution of SWCX emission to the RASS in the direction of the NGPR. While considerable effort was expended to remove non-cosmic backgrounds from the RASS, neither the heliospheric SWCX or the non-time varying component of the magnetosheath SWCX were addressed, as they were unknown at the time. For the residual magnetosheath SWCX we assume the 50 RU as discussed in GEA14. For the heliospheric SWCX contribution we scale the GEA14 results from the direction $l, b \sim 144°, 0°$ to the direction $l, b \sim 305°, 84°$ using the models for the SWCX emissivity from interstellar hydrogen and helium flowing through the solar system (Koutroumpa et al. 2006, see Paper I for more details). As in Paper I and GEA14, we consider the two cases where the ratio of the hydrogen to helium charge exchange X-ray emission efficiency is 1 or 2.

As in Paper I, we define the parameter $\kappa = \beta \int n_{\rm H} R^{-2} dr + \int n_{\rm He} R^{-2} dr = \beta \kappa_{\rm H} + \kappa_{\rm He}$ which is proportional to the SWCX intensity. The integral is along the LOS through the heliosphere, $n_{\rm H}$ and $n_{\rm He}$ are the model space densities of interstellar hydrogen and helium flowing through the solar system, β is the SWCX production efficiency ratio between H and He, and R is the distance from the Sun. The integrals for the $l, b \sim 144°, 0°$ direction during the survey were $\kappa^1_{\rm H} = 0.00610$ cm^{-3} AU^{-1} and $\kappa^1_{\rm He} = 0.01873$ cm^{-3} AU^{-1} while the integrals for the NGPR direction are $\kappa^2_{\rm H} = 0.01407$ cm^{-3} AU^{-1} and $\kappa^2_{\rm He} = 0.01987$ cm^{-3} AU^{-1}, respectively. The heliospheric SWCX scale factor is then: $(\kappa^2_{\rm He} + \beta\kappa^2_{\rm H})/(\kappa^1_{\rm He} + \beta\kappa^1_{\rm H})$, yielding values of 1.37 for $\beta = 1$ and 1.55 for $\beta = 2$. The results are listed in Table 2.

2.5. LHB Emission and Path Length

After subtracting the total SWCX contribution from the fitted foreground emission we are left with LHB emission of 225 ± 38 RU and 208 ± 43 RU for the left side of the region and 121 ± 41 RU and 104 ± 45 RU for the right side. (The paired values are for $\beta = 1.0$ and $\beta = 2.0$, respectively.) As the uncertainties in the LHB emission are a factor of two greater than the difference due to the choice of β, we use the average values 217 ± 43 RU and 113 ± 45 RU for the left and right regions, respectively. (We use the larger uncertainty of the two cases of β as the two samples are not independent.)

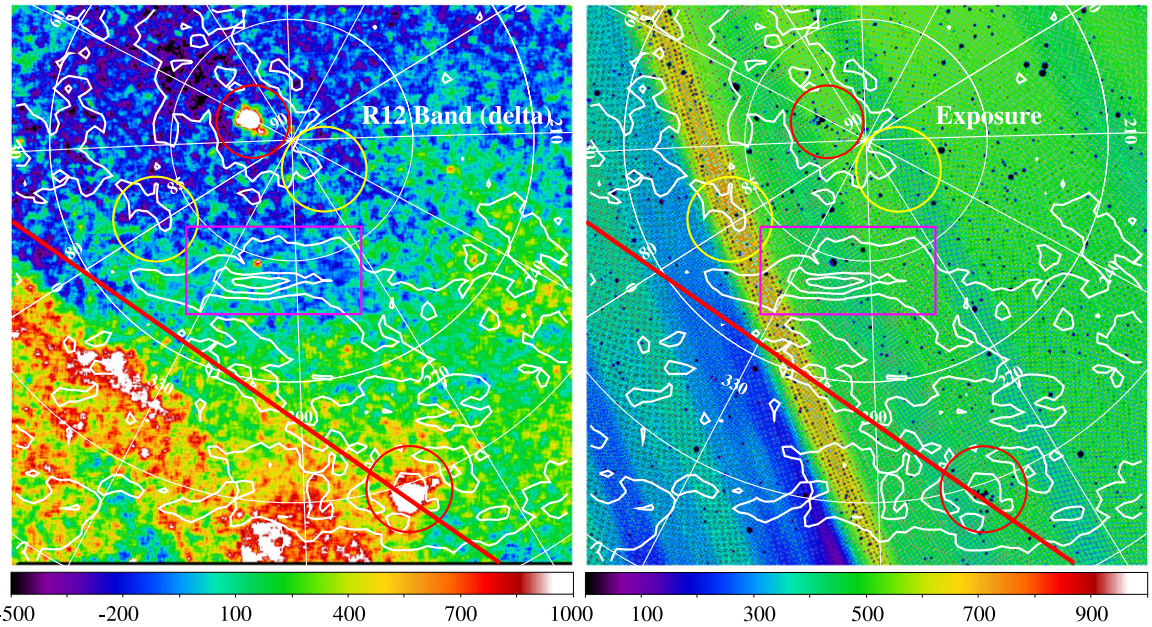

Figure 4. Left: difference between RASS R12 data and the fitted absorption model with the color bar in RU. The strongest positive deviations are in the lower left are from the NPS, along with the Coma and Virgo clusters. Right: the RASS R2 band exposure map for the region in seconds. Note that the scan path ran diagonally between the Virgo and Coma clusters which could have affected the process of modeling and subtracting the SWCX contribution. The contours and regions are the same as in Figure 1.

Table 2
SWCX Parameters

Parameter	Left Half (RU)	Right Half (RU)	β
Foreground Intensity	398 ± 18	294 ± 23	⋯
GEA14 Magnetosheath SWCX	50	50	⋯
GEA14 Heliosphere SWCX	90 ± 25	90 ± 25	⋯
Heliosphere SWCX Scale Factor	1.37	1.37	1.0
⋯	1.55	1.55	2.0
NGPR Magnetosheath SWCX	50	50	⋯
NGPR Heliosphere SWCX	123 ± 34	123 ± 34	1.0
⋯	140 ± 39	140 ± 39	2.0
NGPR Total SWCX	173 ± 34	173 ± 34	1.0
⋯	190 ± 39	190 ± 39	2.0
NGPR LHB Intensity	225 ± 38	121 ± 41	1.0
⋯	208 ± 43	104 ± 45	2.0
Average LHB Intensity[a]	217 ± 43	113 ± 45	⋯

[a] Average intensity for the two cases of β and using the larger uncertainty.

From the results of Snowden et al. (2014), the LHB X-ray emissivity per unit path length is 2.4 ± 0.5 RU pc^{-1} (in good agreement with the derived scale factor of 2.5 RU pc^{-1} from Puspitarini et al. 2014). With the LHB intensities derived above this implies LHB plasma path lengths of 90 ± 27 pc and 47 ± 22 pc for the left and right regions. Because of the likelihood of magnetosheath SWCX over subtraction due to the presence of the Coma and Virgo clusters of galaxies along the scan path covering the right side of the region as discussed above, we consider the left side results to be more reliable, and use them below. Note that this is a conservative choice in that a larger foreground intensity requires a longer path length in the LHB, and therefore be more likely to conflict with the measured distance to the wall of the LC.

The complex of local interstellar clouds (CLICs, e.g., Linsky & Redfield 2014) surrounds the Sun and likely excludes the LHB plasma. This adds another ∼5–10 pc to the required path length from the Sun through the LHB plasma for a total distance of ∼98 ± 27 pc. From Puspitarini & Lallement (2012), the distance to the NGPR is 98 ± 6 pc in remarkably good agreement with the required path length determined from the left region, and easily containing the path length derived from the right region.

3. CONTEMPLATION OF ADDITIONAL DIRECTIONS

In order to apply additional checks on the consistency of the LHB model we have examined a number of additional directions on the sky. To select the directions we used the local ISM maps of Lallement et al. (2014) to search for regions where the LC is bounded by an apparently optically thick distribution of H I. As the resolution of the ISM distribution maps is limited at this time due to the number of sample stars (a limitation that will be resolved by the advent of *Gaia* data, e.g., Perryman et al. 2001; Puspitarini et al. 2015) we examined the RASS 1/4 keV maps to choose directions which also have a constant surface brightness over ∼10°. We also selected a few targets of particular interest: the high latitude molecular clouds MBM 12 and MBM 20 (Magnani et al. 1985) and the H I clouds surrounding the Lockman Hole (Jahoda et al. 1990). Table 3 lists the selected directions.

3.1. Distances to the LC Wall

To determine the distance to the wall of the LC in the selected directions we used published values where available or examined reddening as a function of distance from the work of Lallement et al. (2014). Figure 5 shows the reddening data for the directions (the first 12 in Table 3) converted to an effective column density of H I using the fitted scaling from Figure 2. To

Table 3
Parameters for the Sampled Directions

l (degree)	b (degree)	Distance[a] (pc)	R12 Band (RU)	SWCX (RU)	Plasma[b] (pc)
15	15	78 ± 8	323 ± 2	193 ± 39	56 ± 20
30	0	83 ± 13	320 ± 2	183 ± 36	59 ± 20
45	0	80 ± 25	393 ± 2	177 ± 35	93 ± 24
105	−10	66 ± 19	311 ± 2	160 ± 30	64 ± 19
171	−1	121 ± 34	282 ± 3	143 ± 25	60 ± 17
180	−5	112 ± 22	315 ± 3	154 ± 28	69 ± 19
210	−10	138 ± 18	472 ± 3	142 ± 25	142 ± 31
225	0	133 ± 20	437 ± 3	148 ± 27	124 ± 28
254	33	153 ± 58	460 ± 7	210 ± 44	107 ± 29
315	45	91 ± 28	472 ± 6	178 ± 35	126 ± 30
325	44	88 ± 23	384 ± 5	181 ± 36	87 ± 24
159[c]	−34	88 ± 23	385 ± 7	197 ± 2	78 ± 16
211[d]	−37	130 ± 30	388 ± 7	131 ± 22	110 ± 25
320[e]	83	98 ± 6	407 ± 18	181 ± 35	90 ± 27
224[f]	45	125 ± 25	465 ± 28	194 ± 12	113 ± 28
224[f]	45	17 ± 6	264 ± 31	194 ± 12	29 ± 11
135[g]	51	355 ± 95	662 ± 16	164 ± 22	214 ± 47
144[h]	0	90 ± 15	339 ± 2	136 ± 24	85 ± 15

[a] Distance to the Local Cavity wall.
[b] Plasma path length.
[c] MBM 12 (Snowden et al. 1993).
[d] MBM 20.
[e] NGPR, this work.
[f] Local Leo Cold Cloud (Snowden et al. 2015a).
[g] Lockman Hole clouds (Snowden et al. 1994; Benjamin et al. 1996).
[h] Direction used to determine the distance scale factor (Snowden et al. 2014).

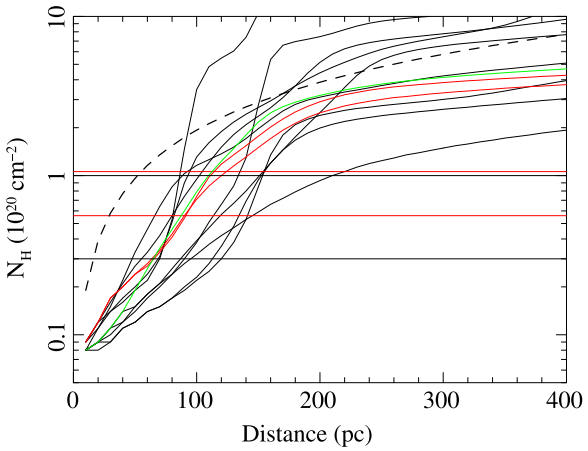

Figure 5. Column density as a function of distance for the first 12 directions listed in Table 3. The two horizontal black lines are at $N_H = 0.3 \times 10^{20}$ and 1.0×10^{20} cm^{-2} which were chosen as the range for the distances to the LC wall. The two horizontal red lines show the equivalent limits for the range in distances using the reddening to column density relation of Paper I. The green curve indicates the MBM12 direction while the red curves indicate the direction that lies on the high side of the distribution in Figure 6 (upper curve) and the nearby direction (see Section 3.4 for details). For comparison, the dashed line shows the integral column density vs. distance expected from a uniform distribution of $n_H = 0.5$ cm^{-3}.

estimate the likely distances to the clouds we use the range in the curves extending between 0.3×10^{20} and 1.0×10^{20} cm^{-2}, and list them in Table 3. As noted above, the scale factor for the Planck reddening map derived in this paper is different from that of Paper I. However, the differences in the 0.3×10^{20}–1.0×10^{20} cm^{-2} range are in most cases relatively minor (see Figure 2) and always in the sense that the Paper I scaling would lead to larger estimates for the distances to the LC wall, and thus less restrictive constraints on the LHB plasma extent. Specifically, if the Paper I relation was used, the equivalent range in Figure 5 would be from 0.56×10^{20} to 1.06×10^{20} cm^{-2} (shown by the horizontal red lines).

For MBM 12 we use a distance to the LC wall of 88 ± 23 pc as derived above, and note that this is significantly less than the distance MBM 12 itself (~160 pc, e.g., Knude & Lindstrøm 2012). MBM 12 is discussed separately below in Section 3.3. For MBM 20, we use the surface brightness from the RASS (MBM 20 appears as a clear shadow) and the distance from Hearty et al. (2000). For the LLCC we use the results from Paper I (and references therein). For the Lockman Hole clouds we used the count rate results from Snowden et al. (1994) and the distance measurement from Benjamin et al. (1996). In addition, we include the results from Snowden et al. (2014) which provided the path length to intensity scaling relation used in this paper.

3.2. RASS Count Rates

Unless specifically noted otherwise, we extracted the R12 band count rates for 4°–10° diameter regions in the selected directions from the data used in Snowden et al. (1997), and list the results in Table 3. The diameters were set by a visual examination of the RASS map to cover the extent of minimum surface brightness associated with the shadow. We assume that the LC wall is optically thick so the extracted values are the sum of only the LHB plasma emission, heliospheric SWCX emission, and magnetosheath SWCX emission. As with the NGPR analysis, the two SWCX components must be modeled and subtracted to isolate the LHB component and estimate the plasma path length. To model the SWCX contribution we use the same process as discussed in Section 2.4. Table 3 lists the total SWCX flux consisting of the heliospheric contribution scaled from the results of GEA14 and an assumed 50 RU from the magnetosheath, except for the LLCC and MBM 12. The magnetosheath contribution for the LLCC and MBM 12 was calculated from the IMP-8 and *ROSAT* pointed observation data (see Section 3.3 for details).

3.3. MBM 12

The high-latitude molecular cloud MBM 12 has appeared many times associated with analysis of the LHB (e.g., Smith et al. 2005; Koutroumpa et al. 2011). Snowden et al. (1993) used a *ROSAT* pointed observation to determine an emission measure scaling for the plasma of the LHB and from that derived a measure of the thermal pressure. However, the distance to MBM 12 has changed significantly over time from the ~65 pc of Hobbs et al. (1986) to the current 160 pc of Knude & Lindstrøm (2012). Because of its history we give it special attention.

Snowden et al. (1993) provide a fitted R12 band foreground intensity of 385 ± 7 RU determined from the *ROSAT* pointed observation RP900138N00. Following the method of Section 2.4 for the estimation of the heliospheric SWCX contribution, we have 82 RU (there is only a ~1 RU difference between the estimates using values of β of 1.0 or 2.0 for the relative SWCX production efficiency of H and He). Using the scaling between magnetosheath SWCX and solar wind flux derived in Paper I, 0.37 R12 counts s^{-1} FOV^{-1} (10^8 cm^{-2} s^{-1})$^{-1}$, and a minimum solar wind flux for the

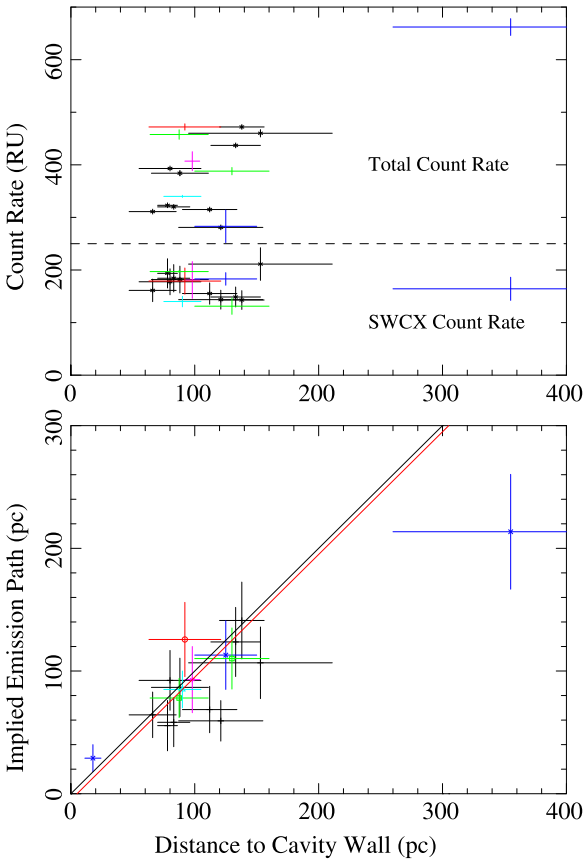

Figure 6. Lower panel: required path length for the LHB plasma to produce the observed LHB flux vs. the distance to the LC wall. The black line indicates equality while the red line is offset by 5 pc to account for the CLICs. The color coding has magenta for the Snowden et al. (2014) results (used for the scaling for all other data), red for the slightly discrepant direction as noted in Figure 5, green for MBM20 (upper) and MBM12 (lower), dark blue for the LLCC data (Snowden et al. 2015a; lower two) and the Lockman Hole clouds (Snowden et al. 1994), and light blue for the NGPR. Upper panel, lower grouping (count rate <250 RU): model SWCX count rate vs. the distance to the LC wall for the directions listed in Table 3. Color assignments are the same as in the lower panel. Upper panel, upper grouping (count rate >250 RU): RASS R12 count rate vs. the distance to the LC wall for the directions listed in Table 3. Color assignments are the same as in the lower panel.

observation interval of 2.0×10^8 cm^{-2} s^{-1} from the IMP-8 data (Frank et al. 1976) accessed through the OMNIWeb Service (King & Papitashvili 2005), we estimate 0.75 counts s^{-1} FOV^{-1} of residual magnetosheath SWCX. Using the scale factor of 156 RU (counts s^{-1} FOV^{-1})$^{-1}$, also from Paper I, we get a final value of 115 RU from the magnetosheath and a total SWCX intensity of 197 ± 2 RU.

The LHB flux foreground to the LC wall in the direction of MBM 12 is then 188 ± 7 RU. Using the same scaling of measured intensity to plasma path length of 2.4 ± 0.5 RU pc^{-1} yields a distance of 78 ± 16 pc. While this value is significantly less than the current distance to MBM 12 of 160 pc, as noted above MBM 12 is likely more distant than the wall of the LC. From the data shown in Figure 5, the distance to the LC wall is 88 ± 23 pc (Table 3).

3.4. Combined Results

Figure 6 (upper panel) shows both the RASS R12 band and model SWCX count rates versus LC wall distance. The RASS data show considerable scatter with the only suggestion of a positive correlation due to the Lockman Hole direction. The model SWCX count rates in the same panel are grouped with perhaps a serendipitous slight negative correlation (the solar system ought not to "know" about the geometry of the LC). However, subtracting the SWCX background from the RASS data and then scaling by the plasma emissivity determined in Snowden et al. (2014) yields a different picture (Figure 6, bottom panel). Although the error bars are relatively large, the data show a strong correlation between the measured distance to the LC wall and the required path length of LHB plasma, even without the Lockman Hole direction. For the case where the cavity wall is optically thick the data points should lie slightly below a zero offset line of slope 1.0 (black line in Figure 6) due to the additional non-plasma pathlength within the CLICs (as suggested by the red line with an offset of 5 RU in Figure 6).

We note that the uncertainties for the implied distances (the vertical errors) are in most cases dominated by the ∼20% uncertainty in the distance scale factor. Thus, the relative vertical uncertainties are much smaller, i.e., any change in the scale factor would move the points as an ensemble. The uncertainties, both vertical and horizontal will be significantly reduced with improved ISM maps enabled by the *Gaia* data. We also note that Benjamin et al. (1996) states that with certain extinction corrections the distance to the Lockman Hole clouds could be as low as 240 pc, placing them right at the lines in Figure 6 (lower panel). Also, the one relatively discrepant point in the same figure (the red point above the lines) lies in the direction of the interior of Loop I (l, $b \sim 315°$, 45°). If the wall separating the LC from the Loop I bubble is not optically thick the observed flux can include emission from the superbubble. On the other hand, an adjacent direction at l, $b \sim 325°$, 44° is consistent with the LHB model. The N_H profiles in Figure 5 of the two directions (red curves) coincide until ∼100 pc where they diverge with the l, $b \sim 325°$, 44° direction running ∼20% higher, only reducing the transmitted R12 band flux by another ∼20% at $N_H \sim 2.5 \times 10^{20}$ cm^{-2}. Points below the lines are not of concern as the LHB plasma need not fill the the entire path length to the LC wall.

4. CONCLUSIONS

This paper presented an analysis of the X-ray emission toward the NGPR and its implications for the LHB model for the origin of the observed 1/4 keV diffuse background. We find that the required path length of X-ray emitting plasma to be 94 ± 27 pc and the total path length adding the local clouds and hot plasma to be 104 ± 27 pc. This is in good agreement with the distance to the NGPR determined to be 98 ± 6 pc.

In addition, we examined a number of other directions within the LC where the walls can be assumed to be optically thick at 1/4 keV, thus effectively isolating emission from the LHB. In agreement with the NGPR results, the additional directions have required plasma pathlengths consistent with the measured distance within the LC, and those distances to the LC wall vary by a factor of two. Including the results from the Lockman Clouds and the foreground emission from the LLCC increases the dynamic range to ∼10. These results provide strong additional support for the LHB model for the local interstellar medium and the origin of the bulk of the observed 1/4 keV background.

S.L.S. would like to thank the l'Observatoire de Paris—Meudon GEPI for their hospitality and support as this paper is based on work which took place while he was a Visiting Scientist in 2014 October–November. D.K. and R.L. would like to acknowledge financial support from the French National Program "Physique Chimie du Milieu Interstellaire" of the Institut National des Sciences de l'Univers (INSU). R.L. and L.P. acknowledge support from the French National Research Agency (ANR) through the STILISM project. The *ROSAT* PSPC data used in the MBM 12 analysis were acquired from the HEASARC archive. The OMNI data were obtained from the GSFC/SPDF OMNIWeb interface at http://omniweb.gsfc.nasa.gov.

REFERENCES

Arnal, E. M., Bajaja, E., Larrarte, J. J., Morras, R., & Pöppel, W. G. L. 2000, A&AS, 142, 35
Arnaud, K. A. 1996, in ASP Conf. Ser. 101, Astronomical Data Analysis Software and Systems V, ed. G. H. Jacoby, & J. Barnes (San Francisco, CA: ASP), 17
Bajaja, E., Arnal, E. M., Larrarte, J. J., et al. 2005, A&A, 440, 767
Benjamin, R. A., Venn, K. A., Hiltgen, D. D., & Sneden, C. 1996, ApJ, 464, 836
Berdyugin, A., & Teerikorpi, P. 2002, A&A, 384, 1050
Borken, R. J., & Iwan, D.-A. C. 1977, ApJ, 218, 511
Cox, D. P., & Snowden, S. L. 1986, AdSpR, 6, 97
Cravens, T. E., Robertson, I. P., & Snowden, S. L. 2001, JGR, 106, 24883
Frank, L. A., Ackerson, K. L., & Lepping, R. P. 1976, JGR, 81, 5859
Freyberg, M. J., & Breitschwerdt, D. 2001, in Astronomische Gesellschaft Meeting Abstracts, Vol. 18, ed. E. R. Schielicke, 104
Galeazzi, M., Chiao, M., Collier, M. R., et al. 2014, Natur, 512, 171
Hartmann, D., & Burton, W. B. 1997, Atlas of Galactic Neutral Hydrogen (Cambridge: Cambridge Univ. Press)
Hearty, T., Fernández, M., Alcalá, J. M., Covino, E., & Neuhäuser, R. 2000, A&A, 357, 681
Hobbs, L. M., Blitz, L., & Magnani, L. 1986, ApJL, 306, L109
Jahoda, K., Lockman, F. J., & McCammon, D. 1990, ApJ, 354, 184
King, J. H., & Papitashvili, N. E. 2005, JGRA, 110, 2104
Knapp, G. R. 1975, AJ, 80, 111
Knude, J., & Lindstrøm, H. E. P. 2012, arXiv:1202.3600K
Koutroumpa, D., Lallement, R., Kharchenko, V., et al. 2006, A&A, 460, 289
Koutroumpa, D., Smith, R. K., Edgar, R. J., et al. 2011, ApJ, 726, 91
Kuntz, K. D., Collado-Vega, Y. M., Collier, M. R., et al. 2015, ApJ, submitted arXiv:5030.4756
Lallement, R. 2004, A&A, 418, 143
Lallement, R., Vergely, J.-L., Valette, B., et al. 2014, A&A, 561, A91
Linsky, J. L., & Redfield, S. 2014, Ap&SS, 354, 29
Magnani, L., Blitz, L., & Mundy, L. 1985, ApJ, 295, 402
Markkanen, T. 1979, A&A, 74, 201
Peek, J. E. G., Heiles, C., Peek, K. M. G., Meyer, D. M., & Lauroesch, J. T. 2011, ApJ, 735, 129
Perryman, M. A. C., de Boer, K. S., Gilmore, G., et al. 2001, A&A, 369, 339
Planck Collaboration, Abergel, A., Ade, P. A. R., et al. A&A, 571, A11
Puspitarini, L., & Lallement, R. 2012, A&A, 545, A21
Puspitarini, L., Lallement, R., Vergely, J.-L., & Snowden, S. L. 2014, A&A, 566, A13
Puspitarini, L., Lallement, R., Babusiaux, C., et al. 2015, A&A, 573, A35
Robertson, I. P., & Cravens, T. E. 2003, JGRA, 108, 8031
Sanders, W. T., Kraushaar, W. L., Nousek, J. A., & Fried, P. M. 1977, ApJL, 217, L87
Smith, R. K., Edgar, R. J., Plucinsky, P. P., et al. 2005, ApJ, 623, 225
Snowden, S. L., Chiao, M., Collier, M. R., et al. 2014, ApJL, 791, L14
Snowden, S. L., Collier, M. R., & Kuntz, K. D. 2004, ApJ, 610, 1182
Snowden, S. L., Cox, D. P., McCammon, D., & Sanders, W. T. 1990, ApJ, 354, 211
Snowden, S. L., Egger, R., Finkbeiner, D. P., Freyberg, M. J., & Plucinsky, P. P. 1998, ApJ, 493, 715
Snowden, S. L., Egger, R., Freyberg, M. J., et al. 1997, ApJ, 485, 125
Snowden, S. L., Freyberg, M. J., Plucinsky, P. P., et al. 1995, ApJ, 454, 643
Snowden, S. L., Hasinger, G., Jahoda, K., et al. 1994, ApJ, 430, 601
Snowden, S. L., Heiles, C., Koutroumpa, D., et al. 2015a, ApJ, 485, 125
Snowden, S. L., Heiles, C., Koutroumpa, D., et al. 2015b, ApJ, 806, 119
Snowden, S. L., McCammon, D., & Verter, F. 1993, ApJL, 409, L21
Sofue, Y. 2000, ApJ, 540, 224
Tanaka, Y., & Bleeker, J. A. M. 1977, SSRv, 20, 815
Wargelin, B. J., Markevitch, M., Juda, M., et al. 2004, ApJ, 607, 596
Welsh, B. Y., Sfeir, D. M., Sirk, M. M., & Lallement, R. 1999, A&A, 352, 308
Welsh, B. Y., & Shelton, R. L. 2009, Ap&SS, 323, 1